

deep pulse-coupled neural networks for diagnosis non-small cell lung cancers classification using ct scans

Journal Title
XX(X):1–12
©The Author(s) 2016
Reprints and permission:
sagepub.co.uk/journalsPermissions.nav
DOI: 10.1177/ToBeAssigned
www.sagepub.com/

SAGE

Abstract

The Non-Small Cell Lung Cancer (NSCLC) is the most common type of lung cancer, comprising about 85% of cases, often treated with surgery, chemotherapy, and radiation. This includes advanced imaging, biopsy, and molecular testing, along with tailored treatments like surgery, radiation, chemotherapy, targeted therapy, and immunotherapy. Continuous monitoring, supportive care, and research for new therapies are crucial. It is necessary to detect NSCLC, so many techniques are implemented. But the existing methods have lot of disadvantages such as over fitting, quality control and limited data availability. To overcome the aforementioned problem, Deep Pulse-Coupled Neural Networks with Multi-axis vision transformer using Bowerbird Optimization Algorithm (DPCNN-MAVT-BOA) is proposed for accurately detecting NSCLC. In this input image is taken from LC25000, TCGA and GEO Dataset For the purpose of denoising and picture enhancement Anisotropic Gaussian side windows Guided Filtering (AGSWGF) is proposed. Following that pre-processed images are segmented using Patch-Based Cross-Layer Non-Local Attenuation based MobileNet (PCLNL-MobileNet). After that feature extraction and classification are done using Deep Pulse-Coupled Neural Networks with Multi-axis vision transformer (DPCNN-MAVT) and optimization are done using Bowerbird Optimization Algorithm (BOA) for detecting tumor and normal conditions of the NSCLC. The efficiency of the proposed DPCNN-MAVT-BOA is analyzed using 3 datasets and attains 99.78% accuracy, 97.29% recall and attains better results compared with the existing methods. The establishment of an accurate and automated approach for classifying different forms of NSCLC may be greatly aided by these results.

Keywords

Non-small cell Lung cancer detection, Anisotropic Gaussian side windows Guided Filtering, Cascaded Residual Deep Capsule Group Neural Networks, Bowerbird Optimization Algorithm

Introduction

Parenchymal cell proliferation that is aberrant and unchecked is the root cause of NSCLC. One of the most prevalent forms of cancer cases is lung cancer. Both the prevalence and death rate from cancer are increasing every day [1]. Lung cancer can be categorized as small cell lung cancer (SCLC) or non-small cell lung cancer (NSCLC) based on histological characteristics [2]. Lung cancer, the most common form of non-small cell lung cancer (NSCLC), is linked to the highest death rate globally. Small cell lung cancer (15%) and non-small cell lung cancer (85%) are the two categories. The two most common forms of non-small cell lung cancer (NSCLC) are lung adenocarcinoma (ADC) and lung squamous cell carcinoma (SqCC). The current treatment for those with advanced SqCC is chemotherapy because molecular medications for lung ADC usually don't work against lung SqCC. Precision medicine depends on quick and non-invasive techniques to differentiate lung SqCC from lung ADC. A thorough examination of tumor heterogeneity has been demonstrated by recent developments in radiomics and machine learning (ML). Deep learning (DL) technology is a desirable alternative since it can automatically identify essential illness traits from medical photos [3-5]. A deadly disease, lung cancer claims the lives of around 1.8 million people each year and accounts for 1.4 million new cases. About 85% of all instances of lung cancer are classified as non-small cell lung cancer (NSCLC), which is further

subdivided into three subtypes: Lung ADenocarcinoma (LUAD), Lung Squamous Cell carcinoma (LUSC), and Lung Large Cell carcinoma (LULC). About 90% of the histological subtypes of NSCLC are accounted for by LUAD and LUSC. Early diagnosis is essential for enhancing therapeutic interventions and raising survival rates. Although they have limitations in detecting lung masses, diagnostic Imaging methods like magnetic resonance imaging (MR), PET/CT, and computed tomography (CT) are recommended. CT, particularly low-dose CT, enables 3D thoracic vision and is sensitive to small, calcified lung masses [6-9]. Lung cancer is the second most common type of cancer worldwide. Incidence and mortality rates for cancer were 2.1 million and 1.8 million worldwide in 2018, respectively, accounting for almost 20% of all cancer fatalities. The five-year survival rate prediction for the early stage ranges from 68 to 92%, and for the extremely late stage, it drops sharply below the 10% threshold at 42%. Thus, to increase a patient's chances of survival and lower treatment costs, lung cancer must be detected and treated early [10-12]. Phase III Non-small cell lung cancer (NSCLC) accounts for thirty percent of cases and is the primary cause of cancer-related deaths globally. With an anticipated 5-year survival range of 13% to 36%, despite improvements in treatment, stage III NSCLC still has a dismal overall prognosis. By avoiding local failures and distant metastases, neoadjuvant Concurrent Chemo Radio Therapy (CCRT) followed by surgery has an

improved overall result. Using 18F-FDG PET/CT imaging, prognostic variables for non-small cell lung cancer have been postulated; however, typical PET parameters only indicate the tumor's total glucose metabolism. Clinical diagnosis and treatment response in There is a strong correlation between non-small cell lung cancer and radiomics, which could be used to extract tumor phenotypic traits. This study evaluates the predictive impact of radiomic features on overall survival in patients with stage III [13–14]. This retrospective study aimed to ascertain the predictive usefulness of the latter by comparing the number of resected metastatic lymph nodes (MLN) from non-small cell lung cancer (NSCLC) using the Pathologic Nodal (PN) category as the current staging approach [15].

Novelty and Contribution

- The Anisotropic Gaussian Side Windows Guided Filtering (AGSWGF) goal is to reduce noise in the input images and improve the quality of the input images.
- Patch-Based Cross-Layer Non-Local Attenuation based MobileNet (PCLNL-MobileNet) intends to remove unneeded parts in order to aid the algorithm in making the best diagnosis possible.
- The objective of employing feature extraction and classification using Deep Pulse-Coupled Neural Networks with Multi-axis vision transformer (DPCNN-MAVT) it is helpful to improve the efficiency of feature extraction and also used for classify the input images. This approach aims to enhance the NSCLC detection and classification of input images, and its parameters are optimizes using a novel BOA.

The section 2 reviews the literature; Section 3 suggests a technique; Section 4 presents the results and comments; and Section 5 concludes with future work.

Literature Survey:

In 2023, Hamed et.al [16] has introduced Lung cancer is the second most common cause of mortality worldwide and one of the worst types of the disease. Accurate and early identification of lung cancer histology is necessary to improve survival rates. Artificial intelligence (AI) can find more cancer cases faster and at a lower cost by automating the diagnosing process. The ability of a CNN model to distinguish between images of benign and malignant lung cancer from digital pathology is evaluated in this work. The accuracy of the model ranged from 99.9% to 100%, which reduced processing time.

In 2023 Halder et.al [17] has introduced the MorphAttnNet, a novel deep learning framework that classifies lung cancer subtypes based on image morphology. The framework accurately captures the morphological changes of lung cancer subtypes through the application of morphological procedures and convolution. The system achieved high sensitivity, specificity, average accuracy, precision, and f1-score of 98.33%, 97.76%, 98.96%, 99.12%, and 98.72%, respectively, using the LC25000

dataset that is open to the public. Additionally, the system performed better than current cutting-edge technologies.

In 2024 Noaman et.al [18] has introduced the artificial intelligence (AI) and histological image analysis, this study explores early cancer diagnosis. To increase classification accuracy, DenseNet201 is combined with color histogram approaches. Support Vector Machines and K-Nearest Neighbors are two of the eight machine learning algorithms that are evaluated in this study. 99.683% accuracy rate on LC25000 and 94.808% accuracy rate on BreakHis are attained by the model. The results show how AI can be used for histopathology analysis and offer recommendations for future developments and practical applications.

In 2023 Cao et.al [19] has introduced The two main challenges in classifying non-small cell lung cancer (NSCLC) are the presence of vast redundant regions and scattered feature regions in pathology imaging. A fine-grained categorization network called the Progressive Jigsaw and Graph Convolutional Network (PJGC-Net) is proposed to overcome these issues. The network consists of two modules: the GCN-Based multi-scale puzzle generating module for fine-grained learning and the Jigsaw supervised progressive training module for removing superfluous sections. Experimental results show that the strategy outperforms other methods of categorization.

In 2024 Zheng et.al [20] has introduced the research is to find a possible molecular target for lung treatment adenocarcinoma that is connected to cancer-associated fibroblasts. Hub gene screening, confirmation of COL11A1's differential expression and survival, and assessment of the relationship between Weighted Gene Co-expression Network Analysis (WGCN) and immune checkpoint genes in human malignancies were all conducted using the Cancer Genome Atlas lung adenocarcinoma dataset.

In 2023 Sultana et.al [21] has introduced finds gene biomarkers for NSCLC prognosis and diagnosis using scRNA-seq data. There were 158 DEGs found, 48 of which were up-regulated and 110 of which were down-regulated. Twelve important genes were found and their prognostic, expression, and diagnostic potential assessed.

In 2023 Dwivedi et.al [22] has introduced the novel deep learning framework powered by AI to find biomarkers for many non-small cell lung cancer subtypes (NSCLC). An auto encoder, a Feed-Forward Neural Network, and a biomarker finding module make up the framework. It was discovered that the biomarkers were significant for classifying NSCLC subtypes, with Multilayer Perceptron attaining a 95.74% accuracy rate. Of the 52 biomarkers, 45 have been published in prior research, while seven are still being investigated for targeted treatment of lung cancer.

In 2024 Wang et.al [23] has introduced a radiomic model that uses CT features to predict tumor mutational burden (TMB) level and response to immunotherapy in non-small cell lung cancer (NSCLC). Utilizing 3D-Slicer software, the model was created. It was then validated using ROC curves

and outside datasets, and its suitability for clinical use was evaluated by decision curve analysis.

In 2023 Guo et.al [24] has introduced the Pericentriolar Material 1 (PCM1)'s function in cancer was investigated in this study by examining 411 lung adenocarcinoma (LUAD) and control samples. It was discovered that, maybe as a result of its antagonistic effects on RHOC, higher levels of PCM1 expression were linked to better survival prospects. It was discovered that PCM1 was mostly expressed in membrane and cytoplasmic components. According to the study, treating patients with elevated PCM1 levels may benefit from the use of targeted and chemotherapeutic medicines.

In 2024 Verma et.al [25] has introduced the gene-disease connections and patient gene expression data are combined, biomedical knowledge bases (KBs) can improve medical diagnostic decision support systems. Using two KBs and four real-world gene expression datasets of influenza-like viruses-induced respiratory viral infections, two algorithms, LOADDx and k-NN, have been examined. When it came to detecting infections within 72 hours, LOADDx achieved an average accuracy of 92.66%, while SCADDx achieved an accuracy of up to 100%. These algorithms beat other machine learning techniques.

In 2024 chen et.al [26] has introduced To find putative biomarkers for non-small cell lung cancer (NSCLC) with R software and machine learning methods. Findings indicated that specific siRNAs reduced the expression of GDF10, NCKAP5, and RTKN2 in A549 and H1975 cells, indicating a potential involvement of resting NK cells, Tregs, and activated dendritic cells in NSCLC. Table1 shows the Summary of the existing methods.

Problem Statement:

Non-Small Cell Lung Cancer (NSCLC) is significant because it presents an opportunity to identify the shortcomings of existing treatments through the development of a highly accurate, dependable, and efficient method. Using datasets such as LC25000, TCGA, and GEO, the proposed Deep Pulse-Coupled Neural Networks with Multi-axis Vision Transformer optimized by Bowerbird Algorithm (DPCNN-MAVT-BOA) seeks to achieve improved detection accuracy, recall, and performance by reducing errors and improving generalization.

Proposed Methodology

In this section, the input data is taken from three dataset such as LC25000 dataset, TCGA dataset and GEO datasets. Then these data are pre-processed using Anisotropic Gaussian Side Windows Guided Filtering (AGSWGF) method. Following that, NSCLC is segmented using the Patch-Based Cross-Layer Non-Local Attenuation based mobilenet (PCLNL-MobileNet) method. Then feature extraction and classifications are done using Deep Pulse-Coupled Neural

Networks with Multi-axis vision transformer (DPCNN-MAVT) method and optimized with Bowerbird Optimization Algorithm (BOA). DPCNN-MAVT-BOA is used for detecting the normal and tumor conditions of NSCLC. Figure 1 shows the Work flow diagram of proposed DPCNN-MAVT-BOA.

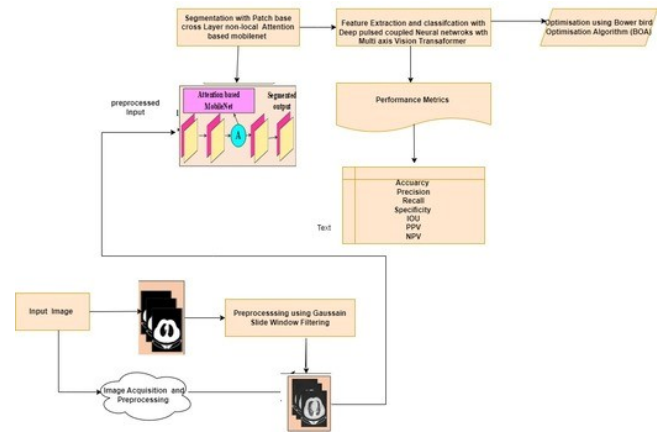


Figure 1. Workflow diagram of proposed DPCNN-MAVT-BOA method

Image Acquisition

In this input images are taken from three datasets such as LC25000 dataset, TCGA dataset and GEO dataset. These images are collected from the thermal images, so that, these images are full of noises, to remove these noises pre-processing techniques are used, they are given below:

Pre-processing using Anisotropic Gaussian Side Windows Guided Filtering (AGSWGF)

Input CT scan images are full of noise so Anisotropic Gaussian Side Windows Guided Filtering (AGSWGF) is used to remove the noises. It entails a number of steps meant to enhance the appropriateness or quality of raw photographs. AGSWGF is an advanced technique utilized in computer vision and image processing for tasks like picture augmentation and denoising. Pixels are either added or subtracted during the image scaling process. Square-sized input photos are preferable since they facilitate a more effective diagnostic process. It extends the traditional guided filtering approach by incorporating anisotropic (direction-dependent) smoothing using Gaussian side windows. Low-pass filtering these data removes these measures entirely, but the averaging step precisely modifies the diffusion level to maintain strong edges. This procedure erodes the edge due to excessive diffusion when is large, while it preserves detail at an edge when is low due to weak diffusion. Let AGSWGF is given in equation (1):

$$R(y, x) = \delta O(y, x) + \frac{\omega_{JO}^{\mu}(y, x)}{\omega_O^{\mu}(y, x)^2 + \epsilon} (J(y, x) - \delta O(y, x)) \quad (1)$$

where, $\sigma_{O(J,x)}$ and $\sigma_{O(O,x)}$ are as defined in the guided filtering, J is the input image, O is the guidance image, μ is the directional information range from 0 to π ,

Table 1. Summary of the existing methods

Reference Number	Methods	Advantages	Disadvantages
16	CNN	High accuracy and comprehensive performance metrics. Combines conventional and deep learning techniques.	May require large annotated datasets, potential overfitting
17	MorphAttnNet	High performance metrics, effective morphological feature extraction.	Complex model, computationally intensive
18	K-NN	High classification accuracy, versatile across different datasets	Potentially high computational complexity, reliance on color histogram
19	PJGC-Net	Effective in handling redundant and scattered feature regions	Complexity of the jigsaw and GCN modules, potential overfitting
20	WGCN	Provides molecular targets for therapy, uses comprehensive dataset analysis	Requires validation in clinical settings, potential for false positives
21	PPIN	Identifies potential biomarkers, uses single-cell RNA sequencing data	Requires further validation, potential complexity in data interpretation
22	FFNN	High accuracy, identifies significant biomarkers	Potentially high computational complexity, reliance on prior research for biomarker validation
23	3D Slicer	Useful for predicting treatment response, validated with decision curve analysis	Requires extensive image processing, potential for overfitting
24	PCM1	Identifies potential therapeutic targets, uses a large dataset	Requires clinical validation, potential for false positives
25	LOADDx	High diagnostic accuracy, effective in real-world datasets	Requires comprehensive biomedical knowledge bases, potential for overfitting
26	SCADDx	High diagnostic accuracy, effective in real-world datasets	Requires comprehensive biomedical knowledge bases, potential for overfitting

$\sigma_{JO(\mu,x)}^d$ is the cross-covariance between J and O computed using the Gaussian side window oriented at angle μ , $\sigma_{O(\mu,x)}^d$ is the standard deviation of O within the same Gaussian side window oriented at angle μ , ε is the numerical stability of a tiny positive constant. The challenge with existing guided filters lies in their inability to fully respect the gradient variations present in the guide image, which can lead to inconsistencies in structure preservation. The covariances between input and guide patches are moderate, resulting in small influence coefficients (b_j). The averaging step rather than solely regulating (b_j) could enhance the degree of anisotropy in these filters. This approach could potentially mitigate the current shortcomings of traditional guided filter variants like AGF, WGIF, and GGIF, thereby improving their effectiveness in handling images with inconsistent structures. A weighted average strategy is given in equations (2-3):

$$\tilde{a}_i = \sum_{i \in M(j)} q_{ji} a_i \quad (2)$$

$$\tilde{b}_i = \sum_{i \in M(j)} q_{ji} b_i \quad (3)$$

where, a_j represents the value or signal at the node or pixel j , $M(j)$ denotes the neighborhood of pixel j which includes all pixels i that are considered adjacent or connected to j in some manner. q_{ji} represents the weight or coefficient associated with the connection or relationship between pixels j and i . b_i is the value or signal at the neighboring pixel i .

Anisotropic Gaussian Side Windows Guided Filtering (AGSWGF) enhances guided filtering by incorporating direction-dependent Gaussian windows. It adapts smoothing to image structures, preserving edges effectively. This method improves image quality by considering anisotropic characteristics of the guidance image, making it suitable for tasks like denoising and enhancement. After that, the segmentation is applied to these previously processed images.

=Segmentation using Patch based Cross-Layer Non-Local Attention based MobileNet (PCLNL-MobileNet)

After preprocessing the input images are given to the segmentation. The segmentation using MobileNet with patch-based Cross-Layer Non-Local Attention. By removing out unneeded parts, image segmentation attempts to aid the algorithm in making the best diagnosis possible. PCLNL-

MobileNet refers to a technique that enhances the Mobile Net architecture with non-local attention mechanisms across different layers, focusing on patches rather than individual pixels. The network can identify long-range connections by calculating the relationships between each pair of places in an input feature map thanks to the non-local attention mechanism. Non-local attention across layers improves feature representation and makes it possible for the model to successfully reflect intricate spatial relationships. By organizing pixels into patches, the patch-based method reduces computational complexity without sacrificing spatial context awareness. The input feature map is given in equation (4):

$$Y \in Q^{H \times W \times C} \quad (4)$$

where, Y denotes the tensor or array variable, Q indicates that Y contains real numbers, H is the height, W is the width, and C is the number of channels, the output feature map X with non-local attention is given in equation (5):

$$X_j = \frac{1}{D_j} \sum_i softmax(g(Y_j, Y_i)) h(Y_i) \quad (5)$$

where, Y_j and Y_i are patches centered around positions j and i , g computes the affinity between patches Y_j and Y_i , h transforms Y_j , $softmax$ computes the attention weights based on the affinity scores, D_i is a normalization factor, mechanism across layers in MobileNet, each layer k computes attention over patches from previous layers is given in equation (6):

$$X_j^{(k)} = \frac{1}{D_j^{(k)}} \sum_i softmax(g(Y_j^{(k)}, Y_i^{(k-1)})) h(Y_i^{(k-1)}) \quad (6)$$

where, $X_j^{(k)}$ denotes the output at position j in layer k , $D_j^{(k)}$ is the normalization factor specific to $X_j^{(k)}$, \sum_i Summation over all indices i , $softmax(\max(g(Y_j^{(k)}, Y_i^{(k-1)})))$ is the Softmax function applied to the affinity or similarity score $g(Y_j^{(k)}, Y_i^{(k-1)})$ between the patch or position j in layer k and the patch or position i in layer $k-1$, $g(Y_j^{(k)}, Y_i^{(k-1)})$ is the affinity function or score that measures the similarity or relationship between the features $Y_j^{(k)}$ at position j in layer k and $Y_i^{(k-1)}$ at position i in layer $k-1$, $h(Y_i^{(k-1)})$ is the transformation function applied to $Y_i^{(k-1)}$. (Eq 6) MobileNet may better comprehend complicated spatial relationships and global context because to the combination of Attention with Patch-Based Cross-Layer Non-Local methods. The model maintains efficiency appropriate for deployment on mobile and embedded platforms, while achieving enhanced performance in tasks such as object detection, semantic segmentation, and picture classification. This is achieved by using non-local attention across layers and concentrating on patches. Then the segmented output is given to the feature extraction.

Feature Extraction and Classification using Deep Pulse-Coupled Neural Networks with Multi-Axis Vision Transformer (DPCNN-MAVT)

After segmented the feature extraction and classification is carried out. Following processing and segmentation of

the raw CT scan pictures, the images undergo an image feature extraction phase where a number of numerical features are extracted. Every pixel in a single image will yield a feature, which will subsequently be saved in a dataset. The Multi-Axis Vision Transformer (MaxViT) for further representation learning and grouping. Deep neural networks are very important in the principal domain of image classification in medical image analysis.

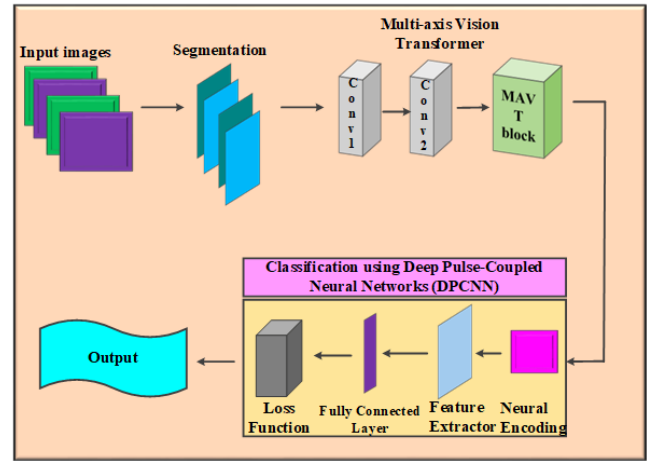


Figure 2. Architecture of Deep Pulse-Coupled Neural Networks - Multi-Axis Vision Transformer (DPCNN-MAVT)

- **Deep Pulse-Coupled Neural Networks (DPCNN)**
DPCNN is a text classification model leveraging convolutional layers with region embedding blocks to extract hierarchical features from text. Every pixel in a single image will yield a feature, which will subsequently be saved in a dataset. A global max-pooling layer consolidates features for classification through fully connected layers, culminating in class predictions via softmax.(Fig 2) DPCNN efficiently learns hierarchical representations, excelling in tasks like sentiment analysis by effectively capturing both local and global textual dependencies. Neural encoding, feature extraction, classifier, and neural decoding are the four components that make up DPCNN.
- **Neural Encoding** Neural encoding converts real valued inputs into spikes, involves transforming the input text into a numerical format suitable for processing by the network. Average pooling is used to prevent severe information loss that may occur with max pooling because of the banality of spikes. This could involve techniques like word embedding's or character embedding's.
- **Feature Extractor** DPCNN uses convolutional layers to extract hierarchical features from the text. A pooling layer is used in the convolutional block to minimize feature map sizes and the location sensitivity of convolutional layers. It employs a specific type of convolutional block called the "region embedding" block. The core idea is to capture local information and gradually aggregate it to form higher-level representations is given in equation (7):

$$x_{k+1} = \alpha(Con(x_k) * Con(x_k)) \quad (7)$$

Where, x_k represents the input feature map at layer k , $Conv(\cdot)$ denotes a convolution operation followed by a non-linear activation, $*$ denotes the max-pooling operation over a fixed-size window, α represents the activation function applied element-wise to the result of the convolution operation $Con(x_k) * Con(x_k)$, x_{k+1} represents the output of the $k - 1$ -th layer in the neural network.

- **Classifier (Fully Connected Layers)** Classifying the retrieved features is subsequently done using a fully connected layer classifier. A global max-pooling operation is carried out following multiple layers of region embedding blocks to produce a fixed-size representation of the complete text. To forecast the probabilities for each class in a classification job, this pooled representation is then fed into fully connected layers and softmax activation is applied after that.
- **Loss Function** The DPCNN's loss function is the temporal efficient training cross-entropy, which can help to increase performance and smooth the loss landscape is given in equation (8):

$$K = \frac{1}{S} \sum_{s=1}^S K_{BF} \left(\text{softmax} \left(P^s \right), x \right) \quad (8)$$

where, K_{BF} signifies loss of cross-entropy, x indicates the target label's single hot coding., P^s shows the synaptic current at a given time step, s of the output non linking DPCNN, the softmax function modifies P^s into a vector of probability \tilde{P}^t , x_j is the true label or target distribution corresponding to time step j , S is the number of time steps or sequence length over which the loss is averaged.

- **Multi-axis Vision Transformer (Max ViT)** The Multi-axis Vision Transformer (Max ViT) is an extension of the traditional Vision Transformer (ViT) architecture designed to improve performance in image classification tasks by incorporating multi-axis attention mechanisms. The Vision Transformer (ViT) revolutionized image classification by applying the transformer architecture directly to image patches. These mechanisms enable the model to capture diverse spatial relationships within image patches, thereby improving its ability to understand and classify images accurately. The attention mechanism in Max ViT computes attention scores is given in equation (9):

$$\text{Attention}(R, L, U) \quad (9)$$

where, $R = YW_r$, $L = YW_l$, $U = YW_u$
where, Y is the input token embedding's, W_r , W_l , W_u are the weight matrices for queries, keys, and values, the attention scores $\text{Attention}(R, L, U)$ adjusted to focus on specific axes is given in equation (10):

$$\text{Attention}(R, L, U) = \text{soft max} \left(\frac{RL^s}{\sqrt{dl}} + B\sigma \right) U \quad (10)$$

where, R , L , U are matrices representing queries, keys, and values, dl is the dimensionality of the keys, B

is an additional matrix that can be used to introduce different attention patterns, σ is the bias parameters.

The first Convolutional block in the study uses a down sampling procedure in its Depth wise Conv3×3 layer. All blocks have 32 attention head size with expansion and shrink rates of 4 and 0.25, respectively. The MaxViT incorporation of both global and local receptive fields and leveraging self-attention mechanisms enhances its ability to analyze CQT (Constant-Q Transform) spectrograms. Then to improve the classification accuracy and to reduce error rate, processing time, complexity and cost of DPCNN-MAVT are optimized using BOA for accurately classifying normal and Tumor Lung Cancer from various datasets. The optimizing process of DPCNN-MAVT is given below:

Optimization using Bowerbird Optimization Algorithm (BOA) In this, BOA is used to optimize the weight parameters of DPCNN-MAVT such as weight for improving accuracy and bias for reducing error rate, processing time, and computational complexity and cost parameter. The Bowerbird Optimization Algorithm (BOA) is named after the bowerbird, which is a bird of prey that attracts mates by building and adorning buildings called bowers. The birds of paradise are closely related to bowerbirds. Native to eastern Australia's rainforests and music woods, bowerbirds are passerines that feed on fruit and insects. They are mostly found in woodlands, and they spend their entire lives in a same locality. Bowerbirds migrate out of their forest habitat into open woodlands in the fall and winter to graze for fruit and insects. That being said, when the spring breeding season approaches, they gather in tiny groups and appear to occupy the same areas every year.

Step1: Initialization

Generate an initial population of Snow geese (possible solutions), with each representing a DPCNN-MAVT set of hyper parameters.

Step 2: Random Generation

Randomly generate the optimization parameters of Bowerbirds to attain the best solution.

Step 3: Fitness function

The fitness function is used to predict the objective function, which is to correctly classify the malignant and non-cancerous zones. It is given in equation (11):

$$\text{Fitness Function} = \text{Minimize } (\sigma), \text{Maximize } (W) \quad (11)$$

where, σ is used for reducing error rate, processing time, computational complexity and cost, W is used to improve accuracy.

Step 4: Elitism (Exploration) for improving accuracy

Elitism is a mechanism commonly used in evolutionary algorithms, including met heuristic algorithms like the Bowerbird Optimization Algorithm (BOA), to ensure that the best solutions discovered so far are preserved across generations. It promotes the retention of high-quality

solutions (also known as elites) from one generation to the next, preventing the algorithm from losing its best solutions due to the randomness of mutation or crossover operations is given in equation (12):

$$Y^{(s)} = \left\{ y_j^{(s)} \right\}_{j=1}^M \quad (12)$$

where, s represents the current iteration or generation of the algorithm, $Y^{(s)}$ is the entire set of the solutions considered by the algorithm at iteration s, j is the index indicating the position of the solution within the population $Y^{(s)}$, $y_j^{(s)}$ is the j-th solution in the population at $Y^{(s)}$ iteration s, $\left\{ y_j^{(s)} \right\}_{j=1}^M$ denotes the collection of all M solutions $y_j^{(s)}$ within the population $Y^{(s)}$.

Step 5: Mutation (exploitation) for reducing error rate,

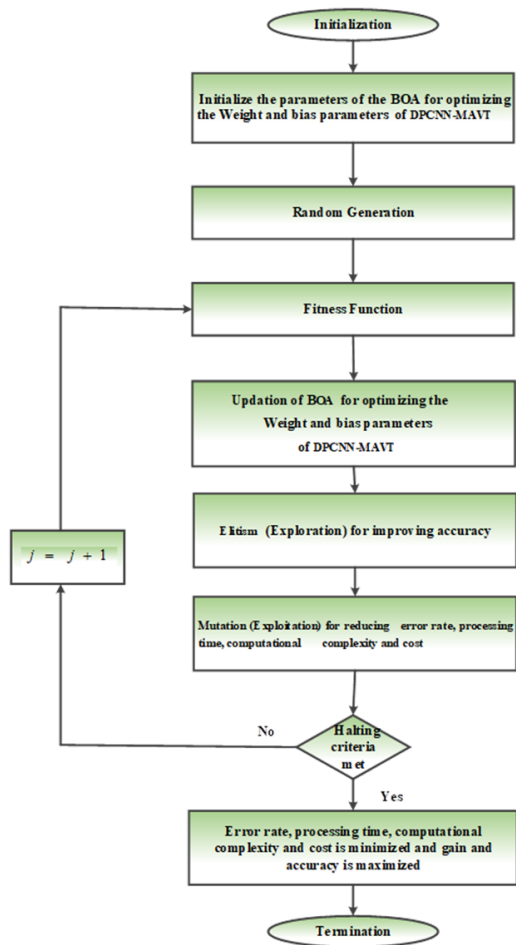


Figure 3. Flow chart of BOA

processing time, computational complexity and cost

Males who are engaged in constructing a ground-level bower run the risk of being attacked by other animals or receiving no attention at all. At the conclusion of every algorithmic cycle, random modifications are implemented with a specific likelihood. Mutation typically involves randomly modifying one or more components (genes) of a solution to explore neighboring solutions that may not be directly reachable through crossover or other operation is given in equation (13):

$$y_{jl}^{\text{new}} \sim M(y_{jk}^{\text{old}}, \mu^2) \quad (13)$$

where, y represents a variable, new denote something new or different, jl be a subscript or an index, ~ symbol usually means negation, M(y) be a function or predicate involving y, μ^2 denote variance.

The value of μ is proportional to the space width is given in equation (14):

$$\mu = x \times (\text{var}_{\max} - \text{var}_{\min}) \quad (14)$$

where, μ represents the standard deviation or possibly another measure of dispersion, x coefficient or factor that scales the difference between var_{\min} and var_{\max} , var_{\max} denotes the maximum value or upper limit of some variable, var_{\min} denotes the minimum value or lower limit of the same variable.

Step 6: Termination

Once the best answers are obtained using equations (11–13), end the operation. Additionally, equation (11) yields the most accurate answer, whereas equation (13) minimizes error rates, processing times, computing complexity, and cost. This iteration is continuing until the halting criteria $j = j + 1$ is met. Finally, the proposed DPCNN-MAVT-BOA accurately classifies the Non-Small Cell lung Cancer as normal and Tumor. (Fig 3)

Result and Discussions

This section describes the introduced scheme's findings and debate. Python is used to carry out the Result and discussion of the method. Here is some of the Implementation parameter is mentioned in table 2:

Dataset Description:

To classify the NSCLC, three NSCLC datasets are taken; they are LC25000 dataset, TCGA dataset and GEO datasets its descriptions are given below:

LC25000 dataset: Five thousand pictures of every kind of lung and colon cancer can be found in the LC25000 collection. The dataset satisfies HIPAA regulations and has been verified. There were only 750 original photographs collected in all, 250 of which were assigned to each category and measured 1024 x 768 pixels. Python is used to reduce the size of these photos to 768x768 pixels, and the software program augmente is used to increase their size. The LC25000 dataset contains two classes namely benign and malignant.

TCGA dataset [20]: Using the TCGA training dataset (n=62), the tumor regions were identified from each layer of the CT scans of the NSCLC patients. The tumor areas were first manually drawn using 3D Slicer software, and then they were rebuilt in three dimensions. There were 1037 unique radiomics features found in the tumor simulation photos. From these 1037 radiomics features, six major categories were found: first-order, gray level run-length matrix (GLRLM), gray level size zone matrix (GLSZM), gray level co-occurrence matrix (GLCM), neighborhood gray tone difference matrix (NGTDM), and gray level dependence matrix (GLDM). It is further divided into two classes namely, tumor and normal

Table 2. Implementation Parameters

Parameters	Description
Proposed Neural Network	DPCNN-MAVT-BOA
OS	Windows 10
Optimization	BOA
Dataset	LC25000 dataset, TCGA dataset and GEO dataset
Software	Python 3.7
Epoches	3000

GEO dataset: There were 151 healthy human participants in this dataset when they signed up for the research. After enrollment, each person received a virus, H1N1, H3N2, HRV, or RSV are the four types. Patterns of gene expression in both infected and uninfected people were obtained by taking blood samples from them at certain intervals, including prior to inoculation. They are further divided into two classes namely, tumor and normal.

Performance metrics:

The Performance measures such Precision, f1-score, recall, accuracy, Intersection Over Union, specificity, Jaccard index, Dice coefficient, error rate and analysis of proposed algorithm are analyzed the proposed DPCNN-MAVT-BOA method's efficiency is contrasted with a number of current techniques, including CNN [16], MorphAttnNet [17] K-NN [18] PJGC-Net [19] in LC25000 dataset WGCN [20] PPIN [21] FFNN [22], 3D Slicer [23] in the TCGA dataset, and WGCN [20] PCM1 [24] LOADDx [25] SCADDx [26] in the GEO dataset respectively and Table 3 shows the performance metrics and equation. The performance metrics equations are given below:

True positive $\alpha\varphi$: Normal accurately forecasts as normal.

False positive $\alpha\phi$: The false positive misclassifies normal as abnormal.

False negative $\beta\varphi$: The false negative misconstrues an aberrant situation as being common in an unusual way.

True negative $\beta\phi$: Remarkably precise predictions of unnatural.

Intersection over Union (IoU): A statistical measure used to assess the accuracy of an item detector on a certain dataset.

Positive Predictive Value (PPV): The measure of how someone who tests positive for a disease is known as the positive predictive value.

Negative predictive value (NPV): The NPV is defined as the proportion of true negative results in all negative tests. It measures how often a person who tests negative truly does not have the disease. NPV is calculated by dividing the number of true negatives (TN) by the sum of true negatives (TN) and false negatives (FN).

where, Overlap Area represents the segment connecting the ground-truth area with the anticipated area and Union Area represents the area that is included in the predicted area and the ground-truth area, p represents the precision, r represents the recall.(Table 3)

Performance Analysis:

In this section, the performance analysis of the proposed method is related with existing methods. Positive predictive value, negative predictive value, f1-score, IoU, recall,

accuracy, and specificity. The efficiency of the proposed DPCNN-MAVT-BOA method is examined using the proposed algorithm in comparison to some existing methods, including CNN [16], MorphAttnNet [17], K-NN [18], PJGC-Net [19] in the LC25000 dataset, WGCN [20] PPIN [21] FFNN [22], 3D Slicer [23] in the TCGA dataset, and WGCN [20] PCM1 [24] LOADDx [25] SCADDx [26] in the GEO dataset, respectively.

Estimation of performance of the proposed approach:

The performance analysis of the proposed method is clarified in this section. The figure 4 shows the output results of LC25000 dataset with 2 classes such as benign and malignant.

The figure 5 shows the output results of TCGA dataset,

Input	Pre-processing	Segmentation	Classification
			(benign)
			(Malignant)

Figure 4. Output results of LC25000 dataset

which contains 2 Classes such as, two classes namely, tumor and normal.

The figure 6 shows the output results of GEO dataset, which

Input	Pre-processing	Segmentation	Classification
			normal
			Tumor

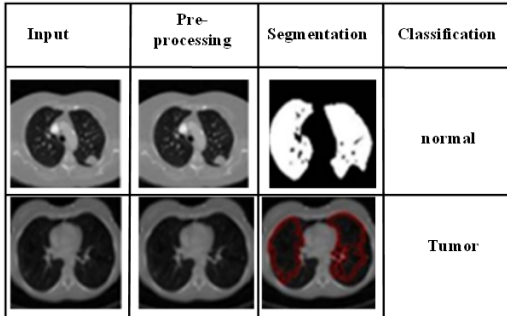
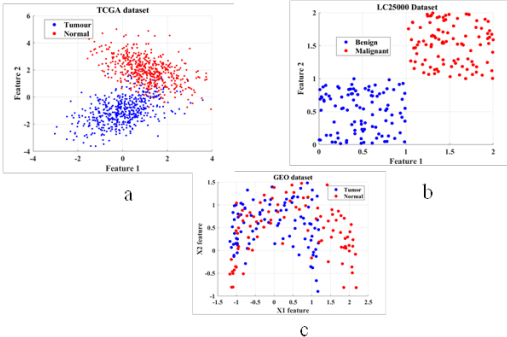
Figure 5. Output results of TCGA dataset

contains 2 Classes such as, two classes namely, tumor and normal.

Figure 7 shows Precision, f1-score, recall, accuracy, Intersection Over Union, specificity, PPV, NPV and error rate analysis for LC25000 dataset, TCGA dataset and GEO datasets and the proposed method is compared with

Table 3. Performance Metrics

Performance metrics	Equation
Precision	$\frac{\alpha\varphi}{\alpha\varphi+\alpha\phi}$
Accuracy	$\frac{\alpha\varphi+\beta\phi}{\alpha\varphi+\beta\phi+\alpha\phi+\beta\varphi}$
Recall	$\frac{\alpha\varphi}{\alpha\varphi+\beta\varphi}$
Specificity	$\frac{\beta\phi}{\beta\phi+\alpha\phi}$
F1-score	$2 \cdot \frac{p \cdot r}{p+r}$
IoU	$\left(\frac{\text{Overlap Area}}{\text{Union Area}} \right)$
PPV	$\frac{\alpha\varphi}{\alpha\varphi+\alpha\phi}$
NPV	$\frac{\beta\phi}{\beta\phi+\beta\varphi}$

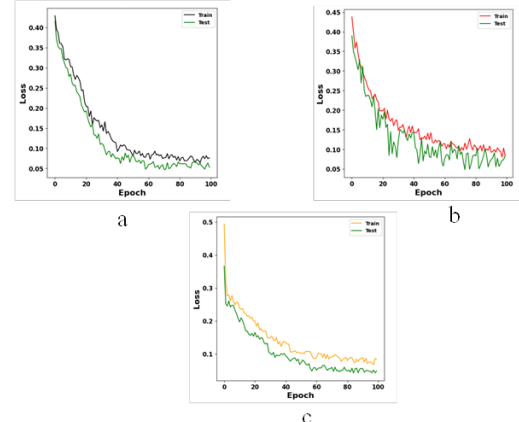
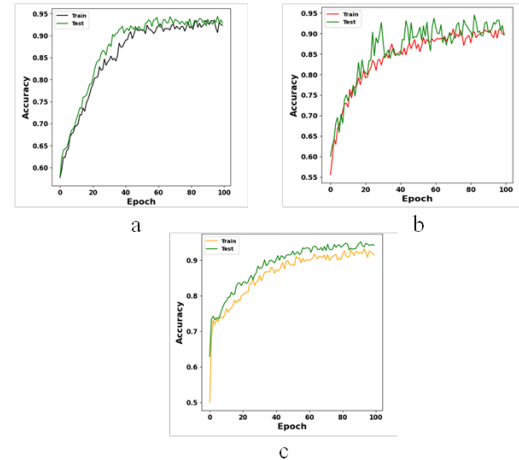
**Figure 6.** Output results of GEO dataset**Figure 7.** Accuracy, specificity, F1-score for (a) LC25000 dataset, (b) TCGA dataset, (c) GEO dataset

existing methods such as CNN[16], MorphAttnNet[17] K-NN[18] PJGC-Net[19] in LC25000 dataset WGCN[20] PPIN[21] FFNN[22] 3D Slicer[23] in TCGA dataset and WGCN [20] PCM1[24] LOADDx [25] SCADDx[26] in GEO dataset respectively. The accuracy of proposed method attains 99.78%, whereas the existing method attains 87.52%, 84.50%, 87.35% and 95.76% respectively for 3 datasets.

Figure 8 shows the performance analysis of Training Accuracy for (a) LC25000 dataset, (b) TCGA dataset, (c) GEO dataset with 99.78% accuracy. By evaluating the model's performance on the training set, training accuracy offers valuable information about how well the model is assimilating the material it has encountered. (Fig 8)

Figure 9 shows the Loss function for (a) LC25000 dataset, (b) TCGA dataset, (c) GEO dataset. One important measure of the model's learning efficiency during training is the loss function. A lower loss function value indicates greater model performance.

Figure 10 shows the ROC curves for the 3 datasets such as LC25000 dataset, TCGA dataset and GEO datasets and

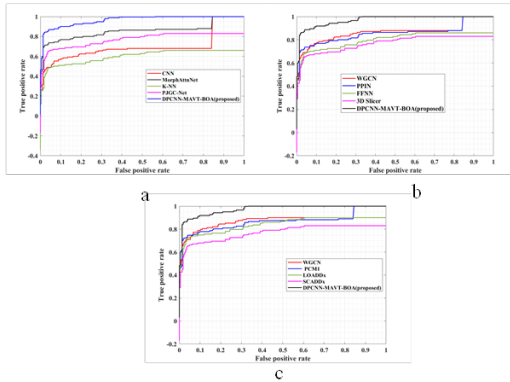
**Figure 8.** (a) Training Accuracy for (a) LC25000 dataset, (b) TCGA dataset, (c) GEO dataset**Figure 9.** Loss function for (a) LC25000 dataset, (b) TCGA dataset, (c) GEO dataset

the proposed method is compared with existing methods such as CNN [16], MorphAttnNet [17], K-NN [18], PJGC-Net [19] in LC25000 dataset WGCN [20] PPIN[21] FFNN [22] 3D Slicer[23] in TCGA dataset and WGCN [20] PCM1[24] LOADDx [25] SCADDx[26] in GEO dataset correspondingly. A graphical representation called a Receiver Operating Characteristic (ROC) curve shows how well a binary classifier system can diagnose problems as its discrimination threshold is changed(Fig 10)

In this section Acc represents accuracy, pre represents the precision, spe represents the specificity, IoU represents

Table 4. Average classifier outcome of DPCNN-MAVT-BOA under varying epochs.

Datasets	Methods (%)	Acc (%)	Pre (%)	Spe (%)	Recall (%)	IoU (%)	PPV (%)	NPV (%)	Error (%)
LC25000 dataset	CNN [16]	87.61	98.5	96.88	96.4	96.77	97.3	89.34	0.5
LC25000 dataset	MorphAttnNet [17]	87.52	76.7	87.9	83.6	90.24	88.6	92.15	0.7
LC25000 dataset	K-NN [18]	86.73	89.6	89.97	89.11	90.23	91.72	92.66	0.4
LC25000 dataset	PJGC-Net [19]	88.69	87.5	86.68	86.68	93.51	89.97	94.29	0.4
TCGA, GEO dataset	WGCN [20]	84.50	91.4	88.4	87.5	91.29	87.4	93.49	0.5
TCGA dataset	PPIN [21]	95.97	99.7	99.7	99.28	99.65	99.47	96.29	0.9
TCGA dataset	FFNN [22]	97.37	89.3	95.1	98.5	86.26	97.43	88.75	0.2
TCGA dataset	3D Slicer [23]	96.52	84.9	92.4	83.9	91.27	94.31	91.24	0.3
GEO dataset	PCM1 [24]	96.45	93.23	78.23	92.34	93.67	94.52	86.25	0.6
GEO dataset	LOADDX [25]	87.35	95.56	94.67	86.67	87.67	90.56	89.37	0.8
GEO dataset	SCADDX [26]	83.39	86.45	89.45	93.34	82.22	84.90	93.45	0.9
LC25000, TCGA and GEO dataset	DPCNN-MAVT-BOA (proposed)	99.78	96.35	99.34	97.29	98.47	96.78	91.34	0.1

**Figure 10.** ROC Curves for (a) LC25000 dataset, (b) TCGA dataset, and (c) GEO dataset

the intersection over union, PPV represents the positive predictive value and NPV represents the Negative Predictive Value.

Table 4 compares the proposed method to existing methods such as CNN [16], MorphAttnNet [17] K-NN [18] PJGC-Net [19] in LC25000 dataset WGCN [20] PPIN [21] FFNN [22] 3D Slicer [23] in TCGA dataset and WGCN [20] PCM1 [24] LOADDx [25] SCADDx [26] in GEO dataset respectively. The proposed technique achieves the best accuracy (99.2%), precision (96.3%), Spe (99.34%), Recall (97.29%), IoU (98.47%), ppv (96.78) and NPV (9134). It also confirms the shortest processing time (0.1) and error rate (0.1) indicating its efficiency and dependability.(Table 4)

Table 5 shows the average classification results of the DPCNN-MAVT-BOA under several epochs.

Ablation study of the proposed method

An ablation study is a methodical experiment carried out to examine the effects of specific elements or characteristics of a suggested approach(Table 5). An ablation study for the suggested method DPCNN-MAVT-BOA would include methodically eliminating or adjusting particular elements or methods in order to determine how they affect the model's overall performance. Table 6 demonstrates the ablation study of the projected method compared with previous Attention networks. From table 6 comparisons of altered configurations of the model and their performance on 3 datasets. The proposed method attains better results by adding Attention with MAVT and Deep Pulse-Coupled Neural Network. Without these networks this method attains less accuracy. The configuration Attention with CNN exhibits a slight drop in accuracy and attains 87.61% for first dataset, 95.97% for second dataset and 87.37% for third dataset. Similarly, the variant Attention with DCNN, with accuracy 99.78% for three datasets. Hence, the proposed Attention with DPCNN-MAVT+BOA attains the accuracy of 99.78%for three datasets respectively.

Conclusion

In this manuscript, the input data is taken from three dataset such as LC25000, TCGA and GEO dataset. Then these data are pre-processed using AGSWGF method. Following that, NSCLC is segmented using the PCLNL- MobileNet. Then the Feature Extraction and classification are done using DPCNN-MAVT for detecting the normal and tumor NSCLC. The introduced system is executed in python. The efficiency of the proposed DPCNN-MAVT-BOA is analyzed using 3 datasets and attains 99.78% accuracy and

Table 5. Average classifier outcome of DPCNN-MAVT-BOA under varying epochs.

No of Epochs	Accuracy (%)	Precision (%)	Specificity (%)	Recall (%)	IoU (%)	PPV (%)	NPV (%)
250	87.61	98.5	96.88	96.4	96.77	97.3	89.34
500	87.52	76.7	87.9	83.6	90.24	88.6	92.15
750	86.73	89.6	89.97	89.11	90.23	91.72	92.66
1000	88.69	87.5	86.68	86.68	93.51	89.97	94.29
1250	84.50	91.4	88.4	87.5	91.29	87.4	93.49
1500	95.97	99.7	99.7	99.28	99.65	99.47	96.29
1750	97.37	89.3	95.1	98.5	86.26	97.43	88.75
2000	96.52	84.9	92.4	83.9	91.27	94.31	91.24
2150	96.45	93.23	78.23	92.34	93.67	94.52	86.25
2300	87.35	95.56	94.67	86.67	87.67	90.56	89.37
2670	83.39	86.45	89.45	93.34	82.22	84.90	93.45
3000	99.78	96.35	99.34	97.29	98.47	96.78	91.34

Table 6. Ablation study

Methods	LC25000dataset	TCGAdataset	GEOdataset
Performance metrics	Accuracy (%)	Accuracy (%)	Accuracy (%)
Attention with DCNN-MAVT	87.61	95.97	87.37
Attention with BOA	87.52	84.50	87.35
Attention with DPCNN-MAVT-BOA	99.78	99.78	99.78

0.1% error rate, compared with the existing methods. This indicates the approach's superior efficiency and potential for further development in the field. Future work will enhance model robustness and generalizability by expanding dataset, integrating real-time processing, and creating a user-friendly interface for detecting the NSCLC.

Acknowledgement. The authors wish to express their heartfelt gratitude to the Department of Computer Science and Engineering, Srm Institute of Science and Technology, for providing the essential resources and infrastructure to carry out this research. We extend our sincere thanks to our colleagues and mentors for their invaluable feedback and guidance, which significantly contributed to the success of this work.

References

- [1] U. Demiroğlu, M. F. Damaşoğlu, A. Öztürk and A. Yazıcı, "Classification of computerized tomography images to diagnose non-small cell lung cancer using a hybrid model," *Multimedia Tools and Applications*, vol. 82, no. 21, pp. 33379–33400, 2023, DOI: 10.1007/s11042-023-15487-y.
- [2] J. Lin, Q. Zhang, X. Li, Y. Wang, and X. Chen, "Classification of histological types and stages in non-small cell lung cancer using radiomic features based on CT images," *Journal of Digital Imaging*, vol. 36, no. 3, pp. 1029–1037, 2023, DOI: 10.1007/s10278-022-00735-6.
- [3] S. U. Atiya, N. V. K. Ramesh, and B. N. K. Reddy, "Classification of non-small cell lung cancers using deep convolutional neural networks," *Multimedia Tools and Applications*, vol. 83, no. 5, pp. 13261–13290, 2024, DOI: 10.1007/s11042-023-15568-y.
- [4] H. A. Helaly, M. E. Shoman, S. A. M. Ghoneim, and M. M. Selim, "ELCD-NSC2: a novel early lung cancer detection and non-small cell classification framework," *Neural Computing and Applications*, pp. 1–16, 2024, DOI: 10.1007/s00521-024-09193-3.
- [5] H. Zhao, L. Liu, W. Zhou, Y. Feng, and Y. Zhang, "Non-invasively discriminating the pathological subtypes of non-small cell lung cancer with pretreatment 18F-FDG PET/CT using deep learning," *Academic Radiology*, vol. 31, no. 1, pp. 35–45, 2024, DOI: 10.1016/j.acra.2023.05.014.
- [6] S. Tomassini, G. Valenti, M. Comparato, M. Indovina, and A. Bertolino, "On-cloud decision-support system for non-small cell lung cancer histology characterization from thorax computed tomography scans," *Computerized Medical Imaging and Graphics*, vol. 110, p. 102310, 2023, DOI: 10.1016/j.compmedimag.2023.102310.
- [7] J. Wang, Y. Zhang, Z. Liu, J. Li, and M. Yang, "CT radiomics-based model for predicting TMB and immunotherapy response in non-small cell lung cancer," *BMC Medical Imaging*, vol. 24, no. 1, p. 45, 2024, DOI: 10.1186/s12880-024-01074-z.
- [8] D. Dora, I. Fekete, T. Kocsis, G. Gálffy, and B. Döbrössy, "Computed Tomography-Based Quantitative Texture Analysis and Gut Microbial Community Signatures Predict Survival in Non-Small Cell Lung Cancer," *Cancers*, vol. 15, no. 20, p. 5091, 2023, DOI: 10.3390/cancers15205091.
- [9] M. Zhu, Y. Lu, Q. Zhang, W. Wang, and H. Li, "Newly diagnosed non-small cell lung cancer with interstitial lung abnormality: prevalence, characteristics, and prognosis," *Thoracic Cancer*, vol. 14, no. 19, pp. 1874–1882, 2023, DOI: 10.1111/1759-7714.15011.
- [10] G. Pasini, A. Corsi, L. Fattori, E. Ambrogi, and M. Bonomo, "Phenotyping the histopathological subtypes of non-small-cell lung carcinoma: how beneficial is radiomics?," *Diagnostics*, vol. 13, no. 6, p. 1167, 2023, DOI: 10.3390/diagnostics13061167.
- [11] A. E. Shevtsov, D. A. Kirsanov, A. V. Pavlov, and D. V. Bugaychenko, "Evaluating the Potential of Metastatic Mediastinal Lymph Node Involvement in Non-Small Cell

- Lung Cancer Patients through Convolutional Neural Networks Analysis of Chest CT," *medRxiv*, 2024, DOI: 10.1101/2024.05.01.24306513.
- [12] N. Chakrabarty, S. Ghosh, P. Sharma, and V. K. Kapoor, "Imaging of brain metastasis in non-small-cell lung cancer: indications, protocols, diagnosis, post-therapy imaging, and implications regarding management," *Clinical Radiology*, vol. 78, no. 3, pp. 175–186, 2023, DOI: 10.1016/j.crad.2022.10.014.
- [13] J. Yoo, H. Kim, Y. Lee, S. Kwon, and S. Park, "Radiomics Analysis of 18F-FDG PET/CT for Prognosis Prediction in Patients with Stage III Non-Small Cell Lung Cancer Undergoing Neoadjuvant Chemoradiation Therapy Followed by Surgery," *Cancers*, vol. 15, no. 7, p. 2012, 2023, DOI: 10.3390/cancers15072012.
- [14] M. Ragab, M. F. Tolba, M. M. A. Salama, and A. E. Hassanien, "Self-Upgraded Cat Mouse Optimizer with Machine Learning Driven Lung Cancer Classification on Computed Tomography Imaging," *IEEE Access*, vol. 11, pp. 36549–36566, 2023, DOI: 10.1109/ACCESS.2023.3256586.
- [15] S. Wei, H. Liu, M. Yu, and X. Zhang, "Which is the better prognostic factor for resected non-small cell lung cancer: the number of metastatic lymph nodes or the currently used nodal stage classification," *Journal of Thoracic Oncology*, vol. 6, no. 2, pp. 310–318, 2011, DOI: 10.1097/JTO.0b013e318206ae90.
- [16] E. A.-R. Hamed, M. M. Aboul Ella, and H. A. Hassanien, "A Deep Learning-Based Classification Framework for Annotated Histopathology Lung Cancer Images," in *Proc. International Conference on Advanced Intelligent Systems and Informatics*, Cham, Switzerland: Springer Nature, 2023, pp. 319–328, DOI: 10.1007/978-3-031-45741-3-30.
- [17] A. Halder and D. Dey, "Morphattnnet: an attention-based morphology framework for lung cancer subtype classification," *Biomedical Signal Processing and Control*, vol. 86, p. 105149, 2023, DOI: 10.1016/j.bspc.2023.105149.
- [18] N. F. Noaman, H. A. Farouk, M. M. E. Haggag, and S. A. Aly, "Advancing Oncology Diagnostics: AI-Enabled Early Detection of Lung Cancer through Hybrid Histological Image Analysis," *IEEE Access*, vol. 12, pp. 45021–45033, 2024, DOI: 10.1109/ACCESS.2024.3389027.
- [19] Z. Cao and W. Jia, "Fine-Grain Classification Method of Non-small Cell Lung Cancer Based on Progressive Jigsaw and Graph Convolutional Network," in *Proc. Chinese Conference on Pattern Recognition and Computer Vision (PRCV)*, Singapore: Springer Nature, 2023, pp. 406–418, DOI: 10.1007/978-981-99-8285-4-33.
- [20] H. Zheng, X. Liu, Y. Zhou, Q. Wang, and J. Zhang, "Analysis of cancer-associated fibroblasts related genes identifies COL11A1 associated with lung adenocarcinoma prognosis," *BMC Medical Genomics*, vol. 17, no. 1, p. 97, 2024, DOI: 10.1186/s12920-024-01735-4.
- [21] A. Sultana, S. Tabassum, M. R. Hasan, and M. A. Islam, "Single-cell RNA-seq analysis to identify potential biomarkers for diagnosis, and prognosis of non-small cell lung cancer by using comprehensive bioinformatics approaches," *Translational Oncology*, vol. 27, p. 101571, 2023, DOI: 10.1016/j.tranon.2023.101571.
- [22] K. Dwivedi, S. Ghosh, A. Das, and A. Ganguly, "An explainable AI-driven biomarker discovery framework for Non-Small Cell Lung Cancer classification," *Computers in Biology and Medicine*, vol. 153, p. 106544, 2023, DOI: 10.1016/j.combiomed.2023.106544.
- [23] J. Wang, Y. Zhang, Z. Liu, J. Li, and M. Yang, "CT radiomics-based model for predicting TMB and immunotherapy response in non-small cell lung cancer," *BMC Medical Imaging*, vol. 24, no. 1, p. 45, 2024, DOI: 10.1186/s12880-024-01074-z.
- [24] Z. Guo, Y. Liu, F. Xu, J. Chen, and H. Yang, "PCM1: A Potential Prognostic Biomarker Correlated with Immune Infiltration in Lung Adenocarcinoma," *Current Proteomics*, vol. 20, no. 3, pp. 208–221, 2023, DOI: 10.2174/157016461966221028102052.
- [25] G. Verma, D. Rebholz-Schuhmann, and M. G. Madden, "Enabling personalised disease diagnosis by combining a patient's time-specific gene expression profile with a biomedical knowledge base," *BMC Bioinformatics*, vol. 25, no. 1, p. 62, 2024, DOI: 10.1186/s12859-024-05677-5.
- [26] K. Chen, H. Li, X. Wu, Z. Wang, and L. Zhou, "Immune infiltration patterns and identification of new diagnostic biomarkers GDF10, NCKAP5, and RTKN2 in non-small cell lung cancer," *Translational Oncology*, vol. 29, p. 101618, 2023, DOI: 10.1016/j.tranon.2023.101618.